

Coupling of terahertz light with nanometre-wavelength magnon modes via spin–orbit torque

Received: 18 May 2022

Accepted: 2 December 2022

Published online: 30 January 2023

 Check for updates

Ruslan Salikhov¹✉, Igor Ilyakov², Lukas Körber^{1,3}, Attila Kákay¹, Rodolfo A. Gallardo⁴, Alexey Ponomaryov², Jan-Christoph Deinert², Thales V. A. G. de Oliveira², Kilian Lenz¹, Jürgen Fassbender^{1,3}, Stefano Bonetti^{5,6}, Olav Hellwig^{1,7}, Jürgen Lindner¹ & Sergey Kovalev²✉

Spin-based technologies can operate at terahertz frequencies but require manipulation techniques that work at ultrafast timescales to become practical. For instance, devices based on spin waves, also known as magnons, require efficient generation of high-energy exchange spin waves at nanometre wavelengths. To achieve this, a substantial coupling is needed between the magnon modes and an electro-magnetic stimulus such as a coherent terahertz field pulse. However, it has been difficult to excite non-uniform spin waves efficiently using terahertz light because of the large momentum mismatch between the submillimetre-wave radiation and the nanometre-sized spin waves. Here we improve the light–matter interaction by engineering thin films to exploit relativistic spin–orbit torques that are confined to the interfaces of heavy metal/ferromagnet heterostructures. We are able to excite spin-wave modes with frequencies of up to 0.6 THz and wavelengths as short as 6 nm using broadband terahertz radiation. Numerical simulations demonstrate that the coupling of terahertz light to exchange-dominated magnons originates solely from interfacial spin–orbit torques. Our results are of general applicability to other magnetic multilayered structures, and offer the prospect of nanoscale control of high-frequency signals.

The increasing demand for fast and energy-efficient communication and data processing stimulates new concepts for terahertz spintronics and magnonics. These concepts require ultrafast (that is, at timescales of picoseconds and below) manipulation of the magnetic spin degree of freedom for the generation of spin currents and short-wavelength magnons at terahertz frequencies^{1–3}. Owing to their terahertz spin dynamics, antiferromagnetic materials have been the particular focus of

research within the past decade^{4–6}. Terahertz spin pumping via antiferromagnetic magnon excitations can also be realized, as demonstrated recently^{7,8}. To generate resonant excitations at terahertz frequencies in technologically relevant metallic ferromagnets, high-energy spin waves have been proposed^{9–14}. In these studies, nanoscale-wavelength spin waves are launched by making use of laser-pulse-driven spin currents—that is, optically induced spin-polarized electrons that move

¹Institute of Ion Beam Physics and Materials Research, Helmholtz-Zentrum Dresden-Rossendorf, Dresden, Germany. ²Institute of Radiation Physics, Helmholtz-Zentrum Dresden-Rossendorf, Dresden, Germany. ³Fakultät Physik, Technische Universität Dresden, Dresden, Germany. ⁴Departamento de Física, Universidad Técnica Federico Santa María, Valparaíso, Chile. ⁵Department of Physics, Stockholm University, Stockholm, Sweden. ⁶Department of Molecular Sciences and Nanosystems, Ca' Foscari University of Venice, Venice, Italy. ⁷Institute of Physics, Chemnitz University of Technology, Chemnitz, Germany. ✉e-mail: r.salikhov@hzdr.de; s.kovalev@hzdr.de

into the interface region of an adjacent ferromagnetic layer. There, the net angular momentum flow creates a spin-transfer torque that acts on the magnetization, consequently exciting high-frequency spin dynamics. As a result, an interface-localized broadband wave packet of nanometre-wavelength magnons launches from the top surface into the depth of the ferromagnetic layer¹¹, followed by its reflection at the layer's bottom surface. This finally results in perpendicular standing spin waves (PSSW), which are detected by using magneto-optical techniques^{9–14}.

Besides optical light, broadband terahertz radiation has been suggested as a means to access ultrafast magnetization dynamics^{15–25}. In this case, the magnetic field component of the terahertz pulse is coherently coupled to the spin system via the Zeeman interaction, and accordingly results in a torque that drives magnetization dynamics at picosecond timescales^{15–24}. However, the excitation of non-uniform and short-wavelength coherent spin waves using a terahertz light source has not been reported yet. This is due to the very inefficient coupling involved, as the momentum of the terahertz light and that of short-wavelength magnons are different by orders of magnitude. Here we overcome this obstacle and demonstrate an efficient and coherent excitation of nanometre-wavelength spin-wave modes in Ta/Py/Pt (where Py is Ni₈₁Fe₁₉) trilayers using a broadband terahertz pulse with about 1 ps duration. Unlike the above-mentioned excitation schemes, the coupling of the terahertz radiation to the spin waves is realized via the spin-orbit torque (SOT)²⁶, which has been predicted to be efficient even at terahertz frequencies^{27,28}. We used a single-cycle terahertz pulse to induce a current in the Ta and Pt metallic layers. This electrical current was then converted into a spin current via the spin Hall effect, which in turn generated a torque acting on the magnetization of the Py layer. Owing to the strong localization of the spin polarization, short-wavelength coherent magnons were excited at the two Py interfaces, and propagated towards each other, resulting in PSSW modes. We demonstrate that the terahertz SOT induces PSSW modes in Py films of 6–12 nm thickness with mode dispersion in agreement with the exchange-dominated analytical relation of the spin-wave-resonance (SWR) frequency $f_{\text{SWR}}(k)$ (Kittel formula) given by:

$$2\pi f_{\text{SWR}} = 2\pi f_0 + (D_{\text{ex}}/\hbar)k^2. \quad (1)$$

In equation (1) f_0 is the uniform mode frequency of the ferromagnetic layer, D_{ex} is the exchange stiffness parameter, \hbar is the reduced Planck constant and $k = \pi n/d_{\text{py}}$ is the wavenumber, which is indexed by the number of nodes, n , in the Py layer of thickness d_{py} . As we show below, no PSSW modes were detected in Ta/Py/Ta and Pt/Py/Pt trilayers with symmetric interfaces, confirming that the direct coupling of the magnetic field of the terahertz radiation to the Py layer cannot be the source of the detected spin waves.

Experiment

To study spin dynamics, we employed time-resolved magneto-optics in a Faraday configuration, as schematically shown in Fig. 1a. An intense single-cycle terahertz pulse is focused onto a trilayer sample and the sample's magnetization state is then probed by polarization rotation of a delayed 100 fs probe pulse with a central wavelength of 800 nm. The terahertz and probe pulses are collinear and have normal incidence with respect to the sample surface. In this configuration, the polarization of the probe pulse is sensitive to the out-of-plane (z axis) magnetization component, which is driven by the terahertz radiation. A more detailed description of the pump-probe experiment is provided in the Methods.

We studied Ta(3 nm)/Py(9 nm)/Pt(2 nm) samples, as shown in Fig. 1a (the thickness of each individual layer is given in parentheses). As reference samples, we also used Ta(3 nm)/Py(9 nm)/Ta(3 nm) and Pt(2 nm)/Py(9 nm)/Pt(2 nm) samples with symmetric interfaces. All samples were deposited on transparent double-sided polished quartz glass, as well as on Al₂O₃ substrates with a substrate thickness of 3 mm.

Different substrates are used to account for the back-reflected terahertz signal in transmission geometry. We employed a 50 mT external magnetic field (\mathbf{H}_{Ext}) to keep the samples magnetically saturated with the magnetization (\mathbf{M}) in the film plane, with the option to make it parallel or orthogonal to the magnetic field component of the incident terahertz pulse (\mathbf{H}_{THz}).

Figure 1b presents a comparison of the time-resolved magnetization dynamics in asymmetric Ta/Py/Pt versus symmetric Ta/Py/Ta samples (the symmetric Pt/Py/Pt sample shows an identical response to the Ta/Py/Ta; see Supplementary Note 1 and Supplementary Fig. 1). A typical coherent response driven by the Zeeman interaction between the Py magnetization and \mathbf{H}_{THz} (seen as a single-cycle transient of about 1 ps duration) is evident for all samples^{17,20–23}. The Zeeman torque-driven magnetization dynamics in the asymmetric and symmetric samples result in a similar signal, which we will refer to as the Zeeman torque signal (ZTS). In contrast to the samples with symmetric interfaces, once the terahertz pulse has passed through the sample, the signal of the Ta/Py/Pt sample clearly exhibits additional features in the form of oscillations at longer delay times (see the black curve in Fig. 1b). The amplitude of the magnetization's precessional signal, A_{SWR} , is about 7.5% of the ZTS amplitude A_{ZTS} for this particular sample, as indicated by the dashed lines in Fig. 1b. The frequency of the oscillations is calculated to be at 0.29 ± 0.01 THz, which we attribute to the SWR mode with $n = 2$ in equation (1). Both the ZTS and SWR show a linear response with respect to the amplitude of the terahertz field (Supplementary Note 2 and Supplementary Fig. 2), indicating that they are not due to the heat deposited by the radiation. Furthermore, the absence of the SWR in the Ta/Py/Ta (and Pt/Py/Pt) sample suggests that \mathbf{H}_{THz} alone cannot be the driving force for the detected spin-wave excitations. In the following, we show instead that the SOT is the mechanism responsible for the observed magnon modes, employing the characteristic symmetry of SOTs induced by the terahertz field.

To confirm that both ZTS and SWR signals from the Ta/Py/Pt sample are magnetic in origin, we present in Fig. 1c the response of the Ta(3 nm)/Py(8.6 nm)/Pt(2 nm) sample with the magnetization aligned perpendicular (black curve) or parallel (red curve) to \mathbf{H}_{THz} . The vanishing ZTS in the parallel configuration indicates its magnetic origin, since the Zeeman torque is zero for a magnetization oriented parallel to \mathbf{H}_{THz} (ref. 23). Similarly, the SOT is inefficient for electrical fields orthogonal to the in-plane magnetization^{26–30}, hence the SWR signal was not detected. We attribute the small ZTS visible in Fig. 1 to a slight misalignment, possibly also due to a non-ideal polarization of the terahertz field. We also checked the effect of reversing the external magnetic field \mathbf{H}_{Ext} on the Faraday signal (Fig. 1d). Both the coherent and the oscillatory responses reversed their sign on reversal of the sign of \mathbf{H}_{Ext} . The sign inversion of the ZTS was expected, as the Zeeman torque is asymmetric under magnetization reversal²³. The asymmetric behaviour of the SWR signal is a further indication that the SOT is the driving mechanism, as we reason below.

To explain the asymmetric behaviour of the SWR signal in Fig. 1d, we start with the Landau–Lifshitz–Gilbert equation:

$$\partial_t \mathbf{m} = -\gamma (\mathbf{m} \times \mathbf{H}_{\text{eff}}) + \alpha \mathbf{m} \times \partial_t \mathbf{m}. \quad (2)$$

In equation (2) $\mathbf{m} = \mathbf{M}/M_s$ is the magnetization unit vector normalized to the magnetization at saturation M_s , γ is the gyromagnetic ratio, t is time and α is the Gilbert damping parameter. The effective field \mathbf{H}_{eff} is given by:

$$\mathbf{H}_{\text{eff}} = \mathbf{H}_{\text{Ext}} + \mathbf{H}_{\text{THz}} + \mathbf{H}_{\text{FL}} + \mathbf{H}_{\text{DL}}, \quad (3)$$

where we consider the SOT-induced field-like \mathbf{H}_{FL} and damping-like \mathbf{H}_{DL} equivalent fields with $\mathbf{H}_{\text{FL}} \propto (\mathbf{z} \times \mathbf{j})$ and $\mathbf{H}_{\text{DL}} \propto (\mathbf{j} \times \mathbf{z}) \times \mathbf{m}$ (refs. 26,29,30). Here \mathbf{j} is the electrical current density induced by the terahertz field

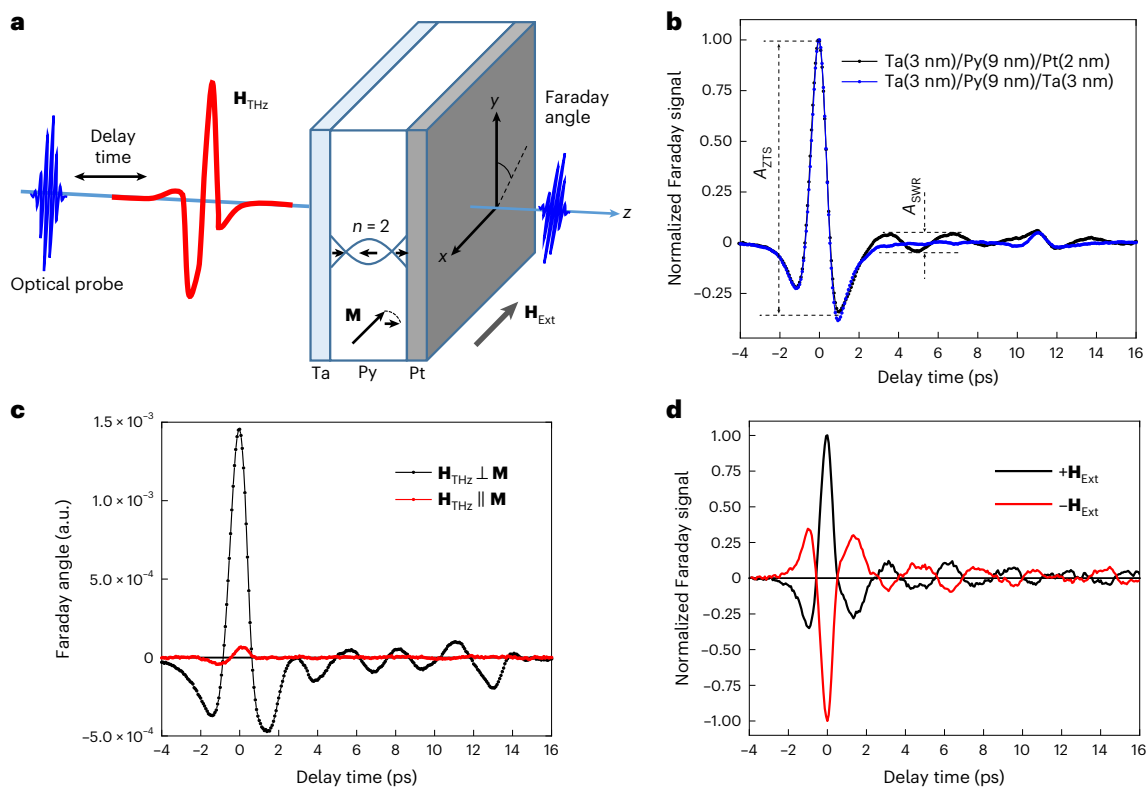


Fig. 1 | Terahertz SWR excitation in a Py layer. **a**, Schematic of the experiment. The single-cycle terahertz pulse is incident on the Ta/Py/Pt sample, which excites standing SWR modes in the Py layer. The z-axis dynamic component of the Py magnetization is detected using a 100 fs laser-probe pulse via the Faraday rotation effect. **b**, Comparison of the magnetization dynamics in two different samples with symmetric (Ta/Py/Ta) and asymmetric (Ta/Py/Pt) interfaces. The spin-wave excitation, which follows the ZTS, is evident (much more pronounced) for the asymmetric sample. **c,d**, Comparison of the magnetization dynamics

in the Ta/Py/Pt sample for Py magnetization aligned perpendicular (black) and parallel (red) with respect to \mathbf{H}_{THz} (**c**) and for different polarities of the external magnetic field (**d**), which is perpendicular to the terahertz magnetic field. The deviations in the precessional oscillation seen at a delay time beyond 11 ps in (**b**) and (**c**) result from back-reflected terahertz radiation of the SiO_2 substrate, which vanishes when we use an Al_2O_3 substrate with larger refractive index in **d**. a.u., arbitrary units.

and \mathbf{z} is the unit vector normal to the sample plane. According to equations (2) and (3), the field-like torque is antisymmetric on inversion of the magnetization, whereas the damping-like torque is symmetric. This points to the fact that the field-like torque is responsible for the terahertz-generated SWR signals, explaining the 180° phase shift in Fig. 1d. The reason for the field-like torque prevailing over the damping-like one in our experiment requires further study. We note, however, that when the magnetization lies in the film plane, \mathbf{H}_{FL} could be much larger than \mathbf{H}_{DL} , in contrast to a canted magnetization state³¹. Finally, we exploited the asymmetry of the field-like torque when the sample was flipped with respect to the incident beam direction. This is shown schematically in Fig. 2a.

According to equations (2) and (3), inverting the order of the Ta/Py/Pt layers with respect to the beam direction should not change the sign of the signals induced by \mathbf{H}_{THz} , whereas \mathbf{H}_{FL} is expected to reverse its direction due to the opposite sign of the spin Hall angle in Ta and Pt, as illustrated in Fig. 2a. Accordingly, opposite directions of the torque would lead to a 180° phase shift in the dynamical components of the magnetization. This scenario is revealed in our experiment in Fig. 2b: when the sample is mounted with the Ta layer side towards the incoming beam, the ZTS induced by \mathbf{H}_{THz} is identical to that observed with the flipped sample (that is, with the Pt layer towards the incoming beam). The SWR signal, however, displays a 180° phase shift, confirming the SOT scenario illustrated in Fig. 2a. Exploiting the opposite symmetry of the two main effects, we could isolate the dynamics of the SOT-induced effect by determining the difference of the signals recorded with the sample mounted in opposite configurations. The difference signal,

shown in the inset of Fig. 2b, reveals clear damped oscillations at a frequency of 0.29 ± 0.01 THz.

The time delay scans of the difference signal for different Py thicknesses are presented in Fig. 3a. All samples displayed damped oscillations, and we fitted our data using a decaying cosine function. The thickest 12 nm Py sample exhibited a more complex dynamical behaviour, therefore the best fit to the curve was achieved using a superposition of three damped cosine functions³²:

$$\psi(t) = \sum_{i=1}^3 a_i e^{t/\tau_i} \cos(2\pi f_i t + \varphi_i) \quad (4)$$

where $\psi(t)$ is the time-dependent difference signal, a_i and φ_i are the initial amplitudes and phases of the i th mode and f_i and τ_i are the frequency modes and characteristic damping times. The inset in Fig. 3b shows the mode frequencies as a function of k^2 for the 12 nm Py sample. The dependence on the wavenumber squared is evident, which we fitted using equation (1). The SWR frequency as a function of Py layer thickness for all Ta/Py (d_{py})/Pt samples is plotted in Fig. 3b. As expected, the frequency increased with decreasing Py thickness and reached 0.6 ± 0.01 THz for $d_{\text{py}} = 6$ nm. The fit using equation (1) revealed that the SWR mode in all samples corresponded to the $n = 2$ mode, and the extracted exchange stiffness was $D_{\text{ex}} = 240 \pm 20$ meV \AA^2 ($A_{\text{ex}} = 8 \pm 0.8$ pJ m^{-1} , where A_{ex} is the exchange constant). This value is similar to that reported previously for thin Py films^{33,34}; furthermore, the fit to the multiple modes of the 12 nm Py sample (inset in Fig. 3b) revealed identical D_{ex} , indicating that the exchange stiffness did not

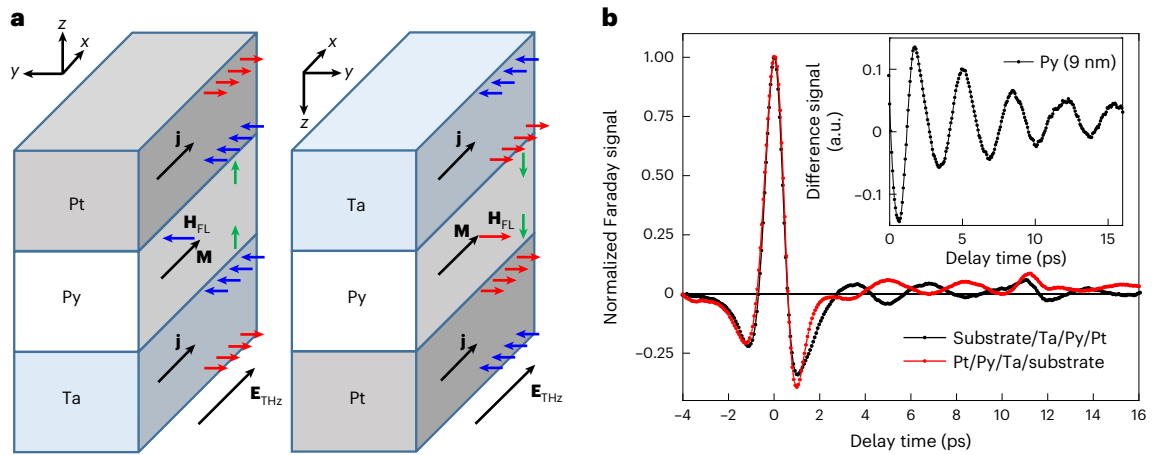


Fig. 2 | Geometry-dependent SOT-driven magnetization dynamics. **a**, The half-period terahertz field E_{THz} generates electrical currents j in the Pt and Ta layers. The spin Hall effect converts the charge currents into respective spin currents, leading to a spin accumulation at the Py interfaces. As Ta and Pt have spin Hall angles of opposite signs, the polarization of the accumulated spins is identical at both interfaces (blue arrows). When the sample is flipped around the x axis (keeping the direction of M constant) the spin accumulation changes sign (red arrows). This results in an opposite direction of the field-like SOT

effective field H_{FL} in these two geometries and, accordingly, opposite torques on M . The z -axis-projected dynamic magnetization components have antiphase time evolution at the interfaces (due to their opposite torques, marked by green arrows), which can be detected by comparing the SWR signals for the two configurations. **b**, Experimental comparison of the magnetization dynamics in the Ta/Pt/Pt sample for the aforementioned configurations. The antiphase behaviour of the SWR signals is evident. The inset shows the difference signal of the black and red curves.

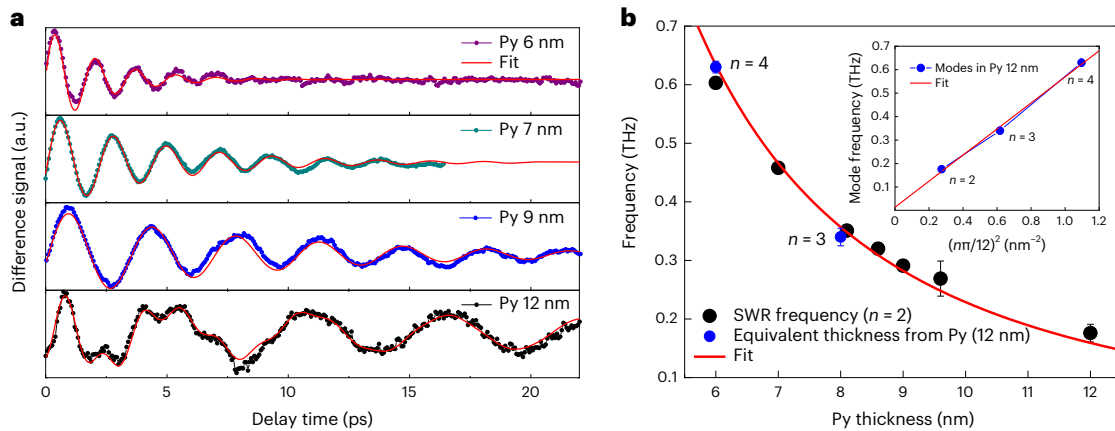


Fig. 3 | Terahertz SWR modes in Py samples with different thicknesses. **a**, Difference time delay scans in Ta/Pt/Pt samples with Py thicknesses of between 6 nm and 12 nm. The presented signals are the result of the difference between two Faraday signals, as previously shown in Fig. 2b. The red lines are the fit to the data points using a decaying cosine function. The 12-nm-thick Py sample exhibits three modes $n = 2, 3, 4$. **b**, Resonance frequency of the $n = 2$ mode as a function of Py thickness (black circles). The blue circles represent the frequency for the equivalent thickness of $n = 3$ and $n = 4$ modes detected in the 12-nm-thick Py

(inset). The equivalent thickness is calculated as a corresponding thickness of $n = 3$ and $n = 4$ modes recalculated to the $n = 2$ mode. The red line is a fit to all data points, representing the universal $1/d^2$ behaviour for $n = 2$ modes in Py films with different thickness, and for different modes in the 12-nm-thick Py. Vertical error bars are extracted from the fitting errors in the analysis of the difference time delay scans using the decaying cosine function. If not otherwise shown, the error bar is smaller than the symbol size.

change much when the Py thickness was decreased down to 6 nm. Modes larger than $n = 2$ became visible in 12 nm Py as the thickness of the metallic sample was comparable to the probe light penetration depth, which was typically 10–15 nm (refs. 35–37). The details of the mode-selective detection in our experiment are discussed below. The relaxation time of the SWR increased with Py thickness. The effective damping parameter of the $n = 2$ mode in the 9 nm Py sample was calculated to be $\alpha_{\text{eff}} = 0.062 \pm 0.002$, which is comparable to the values reported for the PSSW modes at 0.3 THz (refs. 12,13). This value, however, is larger than $\alpha_{\text{eff}} = 0.014$ of the $n = 2$ mode in 50-nm-thick Py³², suggesting a substantial wave number-dependent damping contribution at terahertz frequencies^{12,38,39}.

Micromagnetic modelling

To gain further insight into the origin of the SWR signal in the Ta/Pt/Pt asymmetric system, we modelled the magnetization dynamics microscopically using the MuMax3 code⁴⁰ (see the Methods for details). The magnetic properties of the samples, as well as the asymmetric pinning due to different surface anisotropies at Ta/Pt and Py/Pt interfaces, were extracted from the ferromagnetic resonance characterization discussed in the Supplementary Note 3 and Supplementary Fig. 3. We note that no SWR was obtained in the simulations when a homogeneous or linearly decaying profile of H_{THz} (ref. 22) was assumed within the Py thickness. This also confirmed that the direct action of H_{THz} on the magnetization (Zeeman torque itself) cannot be the origin of the SWR signal.

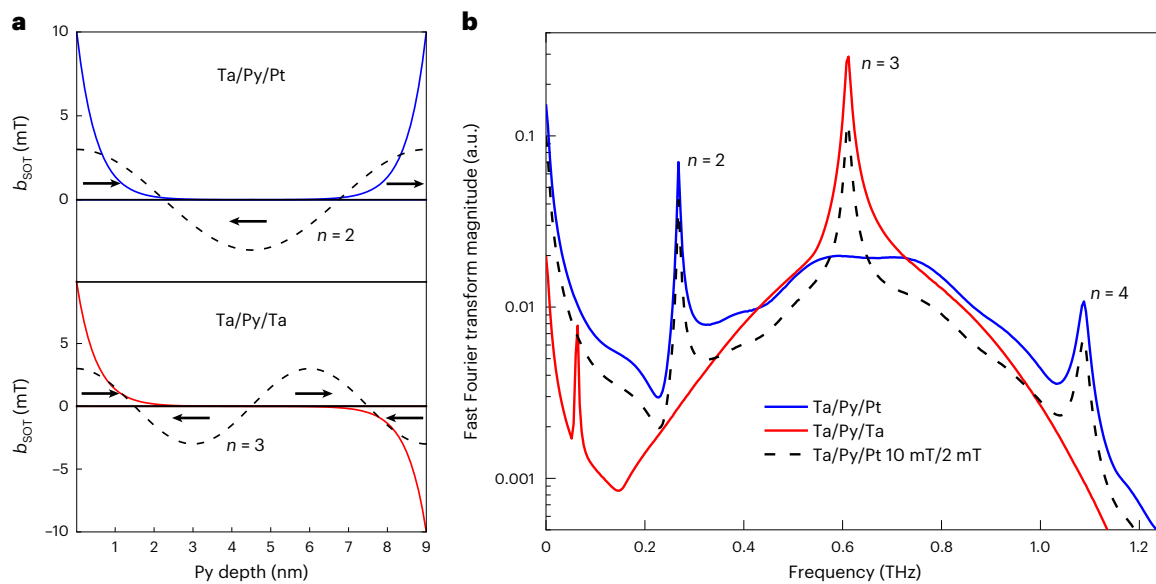


Fig. 4 | Micromagnetic modelling of the SWR excitations. a, Schematic illustration of a 10 mT b_{SOT} field that is localized at a depth of 2 nm at the two interfaces in the asymmetric Ta/Py/Pt (black line, top panel) and symmetric Ta/Py/Ta (red line, bottom panel) samples with 9 nm Py layer. For the asymmetric (symmetric) sample, the SOT fields localized at the two Py interfaces are parallel (antiparallel) with respect to each other. Black arrows illustrate the z-axis-projected magnetization dynamical components across the Py thickness. One can see that the in-phase precession of the magnetization at the two interfaces supports the even- n modes ($n = 2$, black dashed line in the top panel), while the

antiphase precession results in the odd- n modes ($n = 3$, black dashed line in the bottom panel). All modes are unpinned, as the interface anisotropy is not strong enough anymore to pin the exchange-dominated spin waves. **b**, Fast Fourier transform spectra for the magnetization dynamics in the asymmetric Ta/Py/Pt (blue line) and symmetric Ta/Py/Ta (red line) samples. The spectrum for the asymmetric interfaces with different SOT-field amplitudes (10 mT and 2 mT, black dashed line) at the two interfaces demonstrates $n = 2, 3$ and 4 modes. All three modes are detected in the 12-nm-thick sample, where the thickness of the metallic layer is comparable to the probe light penetration depth.

Having verified that the terahertz magnetic field does not contribute to the spin-wave excitation, we estimated the magnitude of \mathbf{H}_{FL} . To do so, we first considered the large refractive index of the metallic films, and calculated the absorbed terahertz power using the transfer matrix method^{41–43}. Next, we estimated the electric current density, which causes the terahertz power absorption (see Supplementary Note 4 and Supplementary Fig. 4 for details). The current density was calculated to be about $j = 10^{12}$ A m⁻². We assumed an SOT efficiency $\mu_0 H_{\text{FL}}/j = 10^{-14}$ T A⁻¹ m² (ref. 26) and, accordingly, arrived at $\mu_0 H_{\text{FL}} = 10$ mT. We further localized the field $b_{\text{SOT}} = \mu_0 H_{\text{FL}} = 10$ mT at the two interfaces of the 9-nm-thick Py layer within a depth comparable to the spin coherence length, as schematically shown in Fig. 4a. The spin coherence length was assumed to be 2 nm, which is a reasonable value for 3d metals and for Py in particular^{39,44,45}. Furthermore, our simulations revealed that the chosen spin coherence length in the interval between 1 nm and 3 nm did not notably influence the SWR amplitudes in the 9 nm Py. Figure 4b plots the simulated spectra for the parallel (as shown in the top panel in Fig. 4a) and antiparallel (bottom panel in Fig. 4a) alignment of b_{SOT} at the two interfaces of the Py layer. The parallel alignment corresponds to the asymmetric Ta/Py/Pt sample, as the opposite sign of the spin Hall angle in Ta and Pt resulted in the same torque direction at both Py interfaces, as schematically shown in Fig. 2a. Accordingly, the opposite direction of the field-like torque in the Ta/Py/Ta sample corresponded to the antiparallel alignment of b_{SOT} . The $n = 2$ mode in the asymmetric sample is evident (blue line in Fig. 4b). Furthermore, as expected, the symmetric sample did not display even- n modes (red line in Fig. 4b), instead $n = 1$ and $n = 3$ modes have substantial amplitudes. These modes were not detected in our experiment as counter-propagating coherent spin waves (which are antiphase and have identical amplitudes) within the transient time of about 2 ps develop standing spin waves with a net-zero dynamical component projected along the z axis. This did not hold for the asymmetric Ta/Py/Pt sample, as the precession amplitudes at the Ta and Pt interfaces were different due to different

SOTs acting on the magnetization. This resulted in an in-depth asymmetrical profile of the dynamical components during the transient time, which was longer than the studied time-delay interval of 25 ps in Fig. 3a. The asymmetrical magnetization profile in turn allowed the detection of the magnetization dynamics in a Faraday geometry. Different magnetization excitation amplitudes at the two interfaces are also expected to result in the odd- n modes. This scenario was verified using micromagnetic modelling by adjusting b_{SOT} at the two interfaces to be 10 mT at the Pt side and 2 mT at the Ta side. The corresponding Fourier spectra are presented in Fig. 4b (dashed black line). Besides the even- n modes, we obtained the $n = 3$ mode with a substantial amplitude. This mode, however, was not detected in the Ta/Py/Pt with 9 nm Py, presumably due to the fact that at 0.6 THz the mode was strongly damped. Additionally, at 0.6 THz, the pump pulse amplitude in the experimental spectral density was about 30% of the peak amplitude at 0.3 THz (Extended Data Fig. 1). The signal from the $n = 3$ mode is therefore expected to be threefold smaller than the signal from the $n = 2$ mode. Furthermore, the asymmetry ratio in b_{SOT} (10 mT/2 mT) at the two interfaces could be smaller, resulting in a smaller amplitude of the $n = 3$ mode. Nevertheless, the higher-order modes ($n = 3$ and $n = 4$) were resolved when the thickness of the Py layer became comparable to the laser-probe light penetration depth in the 12 nm Py sample (Fig. 3).

Discussion

Using time-resolved magneto-optics, we unambiguously demonstrate the efficient excitation of nanometre-wavelength coherent spin waves, driven by terahertz radiation, in a ferromagnetic layer sandwiched by different heavy metals with spin Hall angles of opposite sign. Our experimental and theoretical studies of asymmetric Ta/Py/Pt versus symmetric Ta/Py/Ta systems rule out the possibility that the terahertz magnetic field alone is the source for the SWR, detected in the asymmetric sample. Exploiting the opposite sign of the spin Hall angle in Ta and Pt, and the antisymmetric nature of the field-like torque under

magnetization reversal and sample flipping, we demonstrate that the SOT induced by the terahertz field pulse in the heavy metal layer is the driving force for the terahertz magnons. The efficient excitation of the $n = 2$ mode in the asymmetric Ta/Py/Pt samples is explained by the fact that the magnetization at the two interfaces of the Py layer experiences a torque in the same direction (Fig. 2a). Such in-phase precession at the two interfaces meets the criteria for the observation of the $n = 2$ mode, as schematically shown in the top panel in Fig. 4a. The mode frequency increases quadratically with decreasing Py thickness, according to equation (1), and reaches a maximum of 0.6 THz in 6-nm-thick Py. The lifetime of the 0.6 THz mode is, however, two times shorter than the 0.29 THz mode in 9 nm Py. The decrease of the mode lifetime with frequency is presumably one of the main reasons why the higher harmonic signals (above 0.6 THz) are absent in our experiment. As soon as the laser-probe light penetration depth becomes comparable to the Py thickness in the 12 nm Py, we were able to resolve the $n = 3$ mode. This indicates that the SOT-induced magnetization dynamics amplitudes are different at the Ta and Pt interfaces. The asymmetric torques at two different interfaces are expected, as the SOT efficiency at the Ta interface is usually smaller than at the Pt one²⁶. In the case of symmetric interfaces (that is, in the Ta/Py/Ta sample), the SOT generates counter-propagating coherent magnon packets, which are in antiphase. Consequently, they cancel out each other in the Py layer, and standing spin-wave modes with an even number of n are not excited. The odd-number PSSW modes in the Ta/Py/Ta sample cannot be detected in our experimental geometry for the reasons discussed above. The assumed SOT efficiency $\mu_0 H_{\text{FL}}/j = 10^{-14} \text{ T A}^{-1} \text{ m}^2$ is equivalent to about a $\mu_0 H_{\text{FL}} = 10 \text{ mT}$ field and is assumed to be similar to that in magnetotransport measurements^{26,46} according to the theoretical predictions^{27,28}. We note, however, that the exact verification of the SOT efficiency at terahertz frequencies requires further studies with calibrated Faraday angles using high magnetic fields. These studies are of great interest, as they offer contactless and lithography-free characterization of SOT efficiency in complex heterostructures.

Our work demonstrates the coupling of terahertz light with magnon modes of corresponding energy. Unlike optically induced spin waves^{9–14}, this terahertz-frequency magnon excitation via SOT is linear with the amplitude of the terahertz field, which allows us to achieve coherent and efficient control over the excitation, which is of much fundamental and applied interest. Furthermore, the layered metallic stacks based on an encapsulated ferromagnetic thin film act as an intrinsic terahertz magnon source at zero magnetic field, and offer low-cost fabrication and easy integration into existing technologies^{47–49}, thus opening an attractive pathway towards low-power terahertz-frequency magnonics and spintronics at the nanoscale.

Online content

Any methods, additional references, Nature Portfolio reporting summaries, source data, extended data, supplementary information, acknowledgements, peer review information; details of author contributions and competing interests; and statements of data and code availability are available at <https://doi.org/10.1038/s41567-022-01908-1>.

References

- Kirilyuk, A., Kimel, A. V. & Rasing, T. Ultrafast optical manipulation of magnetic order. *Rev. Mod. Phys.* **82**, 2731–2784 (2010).
- Walowski, J. & Münzenberg, M. Perspective: ultrafast magnetism and THz spintronics. *J. Appl. Phys.* **120**, 140901 (2016).
- Barman, A. et al. The 2021 magnonic roadmap. *J. Phys. Condens. Matter* **33**, 423001 (2021).
- Jungwirth, T., Marti, X., Wadley, P. & Wunderlich, J. Antiferromagnetic spintronics. *Nat. Nanotechnol.* **11**, 231–241 (2016).
- Baltz, V. et al. Antiferromagnetic spintronics. *Rev. Mod. Phys.* **90**, 015005 (2018).
- Hortensius, J. R. et al. Coherent spin-wave transport in an antiferromagnet. *Nat. Phys.* **17**, 1001–1006 (2021).
- Li, J. et al. Spin current from sub-terahertz-generated antiferromagnetic magnons. *Nature* **578**, 70–74 (2020).
- Vaidya, P. et al. Subterahertz spin pumping from an insulating antiferromagnets. *Science* **368**, 160–165 (2020).
- Razdolski, I. et al. Nanoscale interface confinement of ultrafast spin transfer torque driving non-uniform spin dynamics. *Nat. Commun.* **8**, 15007 (2017).
- Lalieu, M. L. M., Helgers, P. L. J. & Koopmans, B. Absorption and generation of femtosecond laser-pulse excited spin currents in noncollinear magnetic bilayers. *Phys. Rev. B* **96**, 014417 (2017).
- Ulrichs, H. & Razdolski, I. Micromagnetic view on magnon generation by femtosecond spin current pulses. *Phys. Rev. B* **98**, 054429 (2018).
- Lalieu, M. L. M., Lavrijsen, R., Duine, R. A. & Koopmans, B. Investigating optically excited terahertz standing spin waves using noncollinear magnetic bilayers. *Phys. Rev. B* **99**, 084439 (2019).
- Choi, G.-M., Lee, D.-K., Lee, K.-J. & Lee, H.-W. Coherent spin waves driven by optical spin-orbit torque. *Phys. Rev. B* **102**, 014437 (2020).
- Brandt, L. et al. Effective exchange interaction for terahertz spin waves in iron layers. *Phys. Rev. B* **104**, 094415 (2021).
- Kampfrath, T. et al. Coherent terahertz control of antiferromagnetic spin waves. *Nat. Photon.* **5**, 31–34 (2011).
- Yamaguchi, K., Nakajima, M. & Suemoto, T. Coherent control of spin precession motion with impulsive magnetic fields of half-cycle terahertz radiation. *Phys. Rev. Lett.* **105**, 237201 (2010).
- Vicario, C. et al. Off-resonant magnetization dynamics phase-locked to an intense phase-stable terahertz transient. *Nat. Photon.* **7**, 720–723 (2013).
- Baierl, S. et al. Terahertz-driven nonlinear spin response of antiferromagnetic nickel oxide. *Phys. Rev. Lett.* **117**, 197201 (2016).
- Baierl, S. et al. Nonlinear spin control by terahertz-driven anisotropy fields. *Nat. Photon.* **10**, 715–718 (2016).
- Bonetti, S. et al. THz-driven ultrafast spin-lattice scattering in amorphous metallic ferromagnets. *Phys. Rev. Lett.* **117**, 087205 (2016).
- Bocklage, L. Model of THz magnetization dynamics. *Sci. Rep.* **6**, 22767 (2016).
- Shalaby, M. et al. Coherent and incoherent ultrafast magnetization dynamics in 3d ferromagnets driven by extreme terahertz fields. *Phys. Rev. B* **98**, 014405 (2018).
- Hudl, M. et al. Nonlinear magnetization dynamics driven by strong terahertz fields. *Phys. Rev. Lett.* **123**, 197204 (2019).
- Blank, T. G. H. et al. THz-scale field-induced spin dynamics in ferromagnetic iron garnets. *Phys. Rev. Lett.* **127**, 037203 (2021).
- Neeraj, K. et al. Inertial spin dynamics in ferromagnets. *Nat. Phys.* **17**, 245–250 (2021).
- Manchon, A. et al. Current-induced spin-orbit torques in ferromagnetic and antiferromagnetic systems. *Rev. Mod. Phys.* **91**, 035004 (2019).
- Guimarães, F. S. M., Bouaziz, J., Dias, M. S. & Lounis, S. Spin-orbit torques and their associated effective fields from gigahertz to terahertz. *Commun. Phys.* **3**, 19 (2020).
- Reiss, D. A., Kampfrath, T. & Brouwer, P. W. Theory of spin-Hall magnetoresistance in the ac terahertz regime. *Phys. Rev. B* **104**, 024415 (2021).
- Garello, K. et al. Symmetry and magnitude of spin-orbit torques in ferromagnetic heterostructures. *Nat. Nanotechnol.* **8**, 587–593 (2013).
- Montazeri, M. et al. Magneto-optical investigation of spin-orbit torques in metallic and insulating magnetic heterostructures. *Nat. Commun.* **6**, 8958 (2015).

31. Avci, C. O. et al. Fieldlike and antidamping spin-orbit torques in as-grown and annealed Ta/CoFeB/MgO layers. *Phys. Rev. B* **89**, 214419 (2014).
32. Salikhov, R. et al. Gilbert damping in NiFeGd compounds: ferromagnetic resonance versus time-resolved spectroscopy. *Phys. Rev. B* **99**, 104412 (2019).
33. Imamura, N. & Chikazumi, S. Determination of exchange stiffness constant using high speed switching of Fe-Ni magnetic thin films. *J. Phys. Soc. Jpn* **25**, 125–132 (1968).
34. Langer, M. et al. Parameter-free determination of the exchange constant in thin films using magnonic patterning. *Appl. Phys. Lett.* **108**, 102402 (2016).
35. van Kampen, M. et al. All-optical probe of coherent spin waves. *Phys. Rev. Lett.* **88**, 227201 (2002).
36. Givens, M. P. Optical properties of metals. *Solid State Phys.* **6**, 313–352 (1958).
37. Bäuerle, D. *Laser Processing and Chemistry* 3rd edn (Springer, 2000).
38. Tserkovnyak, Y., Hankiewicz, E. M. & Vignale, G. Transverse spin diffusion in ferromagnets. *Phys. Rev. B* **79**, 094415 (2009).
39. Li, Y. & Bailey, W. E. Wave-number-dependent Gilbert damping in metallic ferromagnets. *Phys. Rev. Lett.* **116**, 117602 (2016).
40. Vansteenkiste, A. et al. The design and verification of MuMax3. *AIP Adv.* **4**, 107133 (2014).
41. Born, M. & Wolf, E. *Principles of Optics* 6th edn (Cambridge Univ. Press, 1999).
42. Jackson, J. D. *Classical Electrodynamics* 3rd edn (Wiley, 1999).
43. Alber, L., Scalera, V., Unikandanunni, V., Schick, D. & Bonetti, S. NTMpy: an open source package for solving coupled parabolic differential equations in the framework of the three-temperature model. *Comp. Phys. Commun.* **265**, 107990 (2021).
44. Bass, J. & Pratt, W. P. Jr. Spin-diffusion lengths in metals and alloys, and spin-flipping at metal/metal interfaces: an experimentalist's critical review. *J. Phys. Condens. Matter* **19**, 183201 (2007).
45. Ghosh, A., Auffret, S., Ebels, U. & Bailey, W. E. Penetration depth of transverse spin current in ultrathin ferromagnets. *Phys. Rev. Lett.* **109**, 127202 (2012).
46. Nguyen, M.-H., Ralph, D. C. & Buhrman, R. A. Spin torque study of the spin Hall conductivity and spin diffusion length in platinum thin films with varying resistivity. *Phys. Rev. Lett.* **116**, 126601 (2016).
47. Torrejon, J. et al. Neuromorphic computing with nanoscale spintronic oscillators. *Nature* **547**, 428–431 (2017).
48. Seifert, T. et al. Efficient metallic spintronic emitters of ultrabroadband terahertz radiation. *Nat. Photon.* **10**, 483–488 (2016).
49. Makarov, A., Windbacher, T., Sverdlov, V. & Selberherr, S. CMOS-compatible spintronic devices: a review. *Semicond. Sci. Technol.* **31**, 113006 (2016).

Publisher's note Springer Nature remains neutral with regard to jurisdictional claims in published maps and institutional affiliations.

Open Access This article is licensed under a Creative Commons Attribution 4.0 International License, which permits use, sharing, adaptation, distribution and reproduction in any medium or format, as long as you give appropriate credit to the original author(s) and the source, provide a link to the Creative Commons license, and indicate if changes were made. The images or other third party material in this article are included in the article's Creative Commons license, unless indicated otherwise in a credit line to the material. If material is not included in the article's Creative Commons license and your intended use is not permitted by statutory regulation or exceeds the permitted use, you will need to obtain permission directly from the copyright holder. To view a copy of this license, visit <http://creativecommons.org/licenses/by/4.0/>.

© The Author(s) 2023

Methods

Sample fabrication

Samples of Ta(3 nm)/Py(9 nm)/Ta(3 nm) and Ta(3 nm)/Py(d_{py})/Pt(2 nm) where $d_{\text{py}} = 6$ nm, 7 nm, 8.1 nm, 8.6 nm, 9 nm, 9.6 nm and 12 nm were fabricated at room temperature by d.c.-magnetron sputter deposition in a 0.4 Pa Ar atmosphere in an ultrahigh-vacuum BESTEC system. We used 3-mm-thick double-side polished quartz (SiO₂) and sapphire (Al₂O₃) substrates. The thicknesses of all layers were controlled via the deposition time. Before the sample fabrication, the sputter rate of each individual material was calibrated using X-ray reflectivity characterization of the corresponding film. For the magnetic characterization we used a 0.1–50 GHz vector network analyser ferromagnetic resonance set-up.

Pump-probe measurement

In the experiment a laser system with a 1 kHz repetition rate, 1.5 mJ pulse energy, 800 nm central wavelength and 100 fs pulse duration was used. The laser pulses were split into two branches: one for terahertz pulse generation and the other for magneto-optical probing. The first pulse, with a pulse energy of about 1.2 mJ, generated a single-cycle terahertz pulse via a tilted pulse front scheme in a lithium niobate (LiNbO₃) crystal. The terahertz pulse was then refocused onto the sample surface with full-width at half-maximum spot diameter of 0.8 mm and a pulse energy of 2 μJ . The probe pulse was transmitted through the sample and was spatially overlapped with the pump pulse. The temporal delay between the two pulses was controlled using a linear delay stage. The terahertz-induced rotation of the probe pulse polarization was measured with a balanced pair of photodiodes using a half-wave plate and Wollaston prism placed behind the sample.

The peak electric field of (50 ± 5 MV m⁻¹) of the linearly polarized terahertz pulse was measured using electro-optical sampling. The H-field amplitude was estimated to be 160 mT using $B = E/c$, where B is the terahertz induction and c is the velocity of light. All experiments were performed in a dry nitrogen gas atmosphere to suppress absorption of the terahertz radiation by water vapour in air.

Micromagnetic modelling

Micromagnetic simulations were performed using a custom version of the open-source GPU-accelerated micromagnetic solver MuMax3⁴⁰, which relies on the time integration of the Landau–Lifshitz–Gilbert equation of motion of the magnetization on a rectangular grid. The ferromagnetic layers of different thicknesses were modelled using a segment of 3×3 cells in the layer plane and 64 cells along the layer's thickness. The lateral edge length of the cells was set to 5 nm, whereas the cell size along the thickness direction varied between 78 and 203 pm, depending on the chosen layer thickness. To simulate an infinitely extended layer, we applied true periodic boundary conditions in the lateral directions. For the material parameters, we set a saturation magnetization of $\mu_0 M_s = 1$ T, an exchange stiffness constant of $A_{\text{ex}} = 8$ pJ m⁻¹, an out-of-plane anisotropy of $K_u = 25$ kJ m⁻³ and a Gilbert damping constant of $\alpha = 0.01$. Asymmetric surface anisotropy was implemented using additional out-of-plane anisotropies with constants $K_{u,i} = lK_{u,i}$ in only the surface cells of the layer, where l is the cell size along the thickness direction and the surface anisotropy constants $K_{s,1} = 0.1$ mJ m⁻² and $K_{s,2} = 0.2$ mJ m⁻². The in-plane-saturated equilibrium state was found by applying an external magnetic field of $B_{\text{DC}} = 50$ mT. Spin-wave dynamics were excited using a SOT field with a pulse profile:

$$b_{\text{SOT}}(z, t) = [b_p \exp(-\lambda_p z)] \sin(\omega_p t) \exp(-t^2/t_p^2),$$

where the pulse parameters $\omega_p = 4.4$ THz and $t_p^2 = 1.6$ ps² are empirical, fitting the terahertz pump pulse spectrum. The field

b_{SOT} ($b_p = 10$ mT with a skin depth $\lambda_p = 1$ –3 nm, according to the spin coherence length in Py) were applied in the film plane and perpendicular to the direction of magnetization (that is, perpendicular to B_{DC}). The magnetization dynamics was simulated for 250 ps and sampled every 100 fs. Subsequently, a fast Fourier transform of the time evolution of the magnetization was performed for each discretization cell to obtain the spectral response as a sum of all cell contributions.

Data availability

Source data are provided with this paper. All other data that support the finding of this work are available from the corresponding authors upon request.

Code availability

The mathematical code that supports the findings of the study is available via GitHub at <https://github.com/mumax3>. The MuMax3 scripts are provided in Supplementary Code 1.

Acknowledgements

We are grateful to T. Naumann and J. Heinze for experimental and technical support. Parts of this research were carried out at ELBE at the Helmholtz-Zentrum Dresden-Rossendorf e.V., a member of the Helmholtz Association. R.A.G. acknowledges support from Fondo Nacional de Desarrollo Científico y Tecnológico (FONDECYT) under grant agreement no. 1210607.

Author contributions

R.S., J.L. and S.K. conceived and designed the experiment. R.S. and O.H. designed and fabricated the samples. I.I., A.P., J.-C.D., T.V.A.G.d.O. and S.K. carried out the measurements. L.K., A.K. and R.A.G. performed theoretical calculations and micromagnetic simulations. S.B. performed the transfer matrix method calculations. R.S. and K.L. measured and analysed the ferromagnetic resonance. All authors contributed substantially to the discussion and data interpretation. R.S., S.B., O.H., J.L. and S.K. wrote the manuscript with important input from all authors.

Funding

Open access funding provided by Helmholtz-Zentrum Dresden - Rossendorf e. V..

Competing interests

The authors declare no competing interests.

Additional information

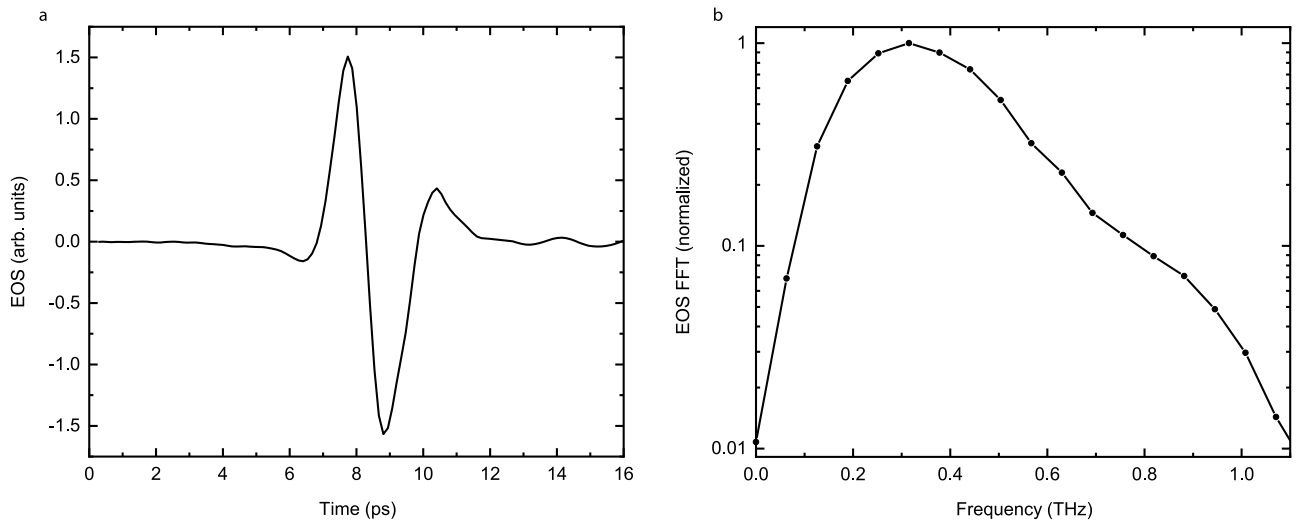
Extended data is available for this paper at <https://doi.org/10.1038/s41567-022-01908-1>.

Supplementary information The online version contains supplementary material available at <https://doi.org/10.1038/s41567-022-01908-1>.

Correspondence and requests for materials should be addressed to Ruslan Salikhov or Sergey Kovalev.

Peer review information *Nature Physics* thanks Akashdeep Kamra and Markus Münzenberg for their contribution to the peer review of this work.

Reprints and permissions information is available at www.nature.com/reprints.



Extended Data Fig. 1 | Temporal and spectral characteristics of THz-pump pulse. a, EOS signal from the broadband THz radiation, displaying the time profile of the single-cycle THz-pump pulse. **b,** Fourier spectrum of the THz pulse normalized to the peak amplitude.